Structural Engineering and Mechanics, *Vol. 61, No. 5 (2017) 593-603*
DOI: https://doi.org/10.12989/sem.2017.61.5.593

Nonlinear simulation of tunnel linings with a simplified numerical modelling

Huiling Zhao[1,2], Xian Liu[*1,3], Yihai Bao[4] and Yong Yuan[1,3]

[1]*State Key Laboratory for Hazard Reduction in Civil Engineering, Tongji University, 1239 Siping Road, Shanghai, China*
[2]*Department of Civil Engineering, Shanghai University, 99 Shangda Road, Shanghai, China*
[3]*Department of Geotechnical Engineering, College of Civil Engineering, Tongji University, 1239 Siping Road, Shanghai, China*
[4]*Department of Civil and Environmental Engineering, University of California, Davis, Davis, California, 95616, USA*

(Received June 5, 2015, Revised October 9, 2016, Accepted October 25, 2016)

Abstract. A high-efficiency simplified modelling approach is proposed for investigating the nonlinear responses of reinforced concrete linings of shield tunnels. Material and geometric nonlinearities are considered in the analysis of the lining structures undergoing large deformation before ultimately losing the load-carrying capacity. A beam-spring element model is developed to capture the force-transfer mechanism between lining segments and radial joints. The developed model is validated by comparing analyzed results to experimental results of a single-ring lining structure under two loading conditions: the ground overloading and the lateral unloading respectively. The results show that the lining structure under the lateral unloading due to excavation on the both sides of the tunnel is more vulnerable compared to the case of ground overloading on the top of the tunnel. A parameter study is conducted and results indicate that the lateral pressure coefficient has the greatest influence on the behaviour of the lining structure.

Keywords: shield tunnel lining; simplified model; radial joint model; nonlinear response

1. Introduction

Shield tunnels have been key elements of the urban infrastructure system. Construction activity in the vicinity of a shield tunnel may result in overloading or unloading to the supporting lining structures, causing adverse deformation in service. Excessive deformations may initiate local structural damage of shield tunnels, such as concrete cracking and spalling, and leakage (Yuan *et al*. 2013). Therefore, understanding the mechanical behaviours of shield tunnels is important for maintaining the serviceability and assuring the safety and repair ability. Due to the complexity and expensive cost for conducting experimental investigations on full-scale lining structures, computational simulations provide an alternate way to study the mechanical behaviours of shield tunnels.

At present, numerical models of shield tunnels can be characterized by following five types: (1) the equivalent uniform beam model, (2) the equivalent stiffness ring model, (3) the hinged joint model, (4) the beam-spring element model, and (5) the shell-spring element model. Shiba *et al*. (1989) proposed the equivalent uniform beam model, where the shield tunnel is treated as a uniform ring in the transverse direction. The equivalent stiffness ring model is an improvement of the equivalent uniform beam model, where an effective stiffness coefficient is employed to consider the influence of the segment joints on the reduction of the ring rigidity. Koyama (2003) developed effective stiffness coefficients of shield tunnels by different joints and different assembly methods in Japan. The hinged joint model is characterized by the fact that all segment joints are regarded as hinges. Due to the existence of multiple hinges, the ring is not a statically determinate structure. However, it is statically determinate with regards to the action of the surrounding rock. Therefore, it is generally used in cases with steady ground conditions. In the beam-spring element models, the segments are assumed as straight or curved beam elements and the segment joints and ring joints are represented by rotational springs and shear springs, respectively. The reduction of the lining stiffness and its influence on the mechanical behaviour of the lining can be captured reasonably well in such a model. Koyama *et al*. (1997) reported a numerical analysis for two parallel tunnels, by using the beam-spring model. Based on the beam-spring model, the shell-spring element model was developed by replacing beam elements with shell elements (Tiberti *et al*. 2008, Naggar *et al*. 2008, Ding *et al*. 2004). It is a big challenge to determine the proper spring properties in beam-spring or shell-spring models, may heavily rely on calibrations (Vardakos 2012).

The present work describes a simplified nonlinear model for a single-ring reinforced concrete lining structure. This model can potentially be extended to model a shield tunnel with multiple rings. In the proposed model, the force transfer at segmental joints is captured by multiple springs representing the contact between the segmental blocks and tensile forces developed in the joint bolts. The model is validated by comparing computed results to experimental results of a full-scale single-ring lining structure. A parametric study is conducted to identify the factors that influence the behavior of the lining structure under overloading and lateral unloading conditions.

∗Corresponding author, Associate Professor
E-mail: xian.liu@tongji.edu.cn

Copyright © 2017 Techno-Press, Ltd.

ISSN: 1225-4568 (Print), 1598-6217 (Online)

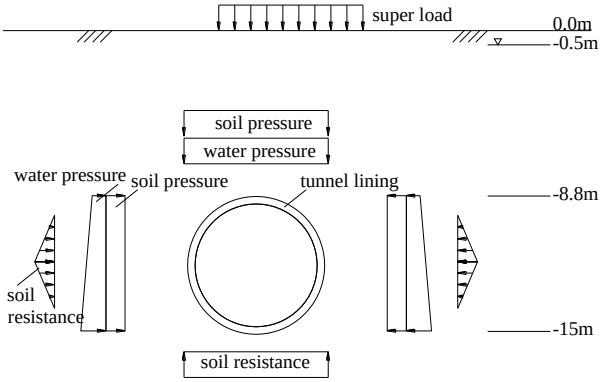

Fig. 1 Overview of the subway shield tunnel in Shanghai

2. Full scale experiment of segmental tunnel lining

A full scale test of a single-ring lining structure was conducted and the measured data are used to validate the proposed model. The test is to simulate a subway shield tunnel in Shanghai with 8.8 m overburden soil. The ground layer is mainly composed of silty clay and oozy soft clay. Water level is 0.5 m below the ground-surface. The pressure loads on the segmental tunnel lining are shown in Fig. 1. The thickness of the lining is 0.35 m. The lining segments were prefabricated with C50 concrete. The Grade 5.8 bolts are used to connect the lining segments at radial joints. Design details can be found at the reference by Liu (2015).

As shown in Fig. 2(a), the outer diameter of the tunnel lining is 6200 mm and the inner diameter is 5500 mm. The width of the segment is 1200 mm. A single-ring lining structure consists of six segments, including the top segment (F), two contiguous segments (L1 and L2), two standard segments (B1 and B2), and the bottom segment (D). The central angle of segment F is 16°, and the central angle of L1, L2, B1, and B2 are 65°. A total of twelve bolts were used to connect the segments, i.e. two bolts in each radial joint.

Hydraulic jacks were used to apply 24 point loads on the exterior surface of the lining structure to simulate soil resistance, soil and water pressure, and ground overload. The point loads are divided into three groups with different assigned values; $P1$ (six point loads), $P2$ (ten point loads), and $P3$ (eight point loads), as shown in Fig. 2(b). $P1$ represents the ground overload including the overburden pressure and the super load. The ratio of $P2$ to $P1$ is determined as a mean lateral pressure coefficient of 0.65. The increase of $P2$ is limited by the passive earth pressure, so the maximum value of $P2$ is no more than 27 5kN. $P3$ is defined as the average value of $P1$ and $P2$. The values and applying points of $P1$, $P2$, and $P3$ are determined so that the pressure and internal forces are in accordance with those of an actual tunnel structure analyzed by the method in Fig. 1. The effect of the soil on the structure is considered as loads applied on the structure.

The experiment of the segmental lining was carried out at the structural engineering laboratory of Tongji University, Shanghai. The test setup shown in Fig. 3 was a self-balanced loading system. It included fixed beams, jacks, distributing beams and anchor bars. All 24 60mm-diameter

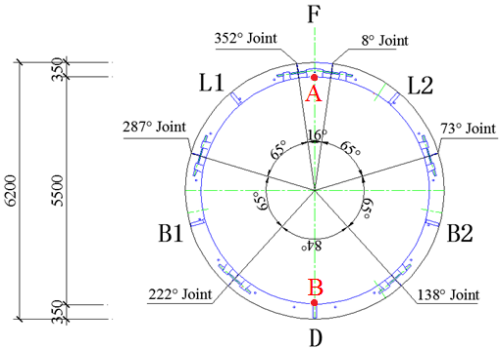

(a) Cross section of the tunnel lining specimen

(b) Loading plan

Fig. 2 Specimen cross section and load plan for the segmental tunnel (unit: mm)

(a) Photo

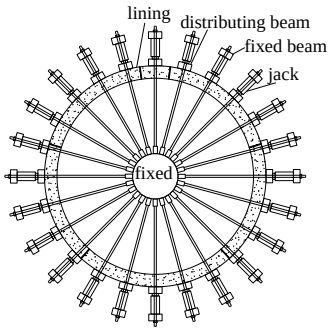

(b) Schematic

Fig. 3 Test setup of the segmental lining

steel bars were fixed at the centre of the lining. As for each point loading, the beam anchored to end of the bar supplied the counter of jack.

The tunnel lining was first tested under load control

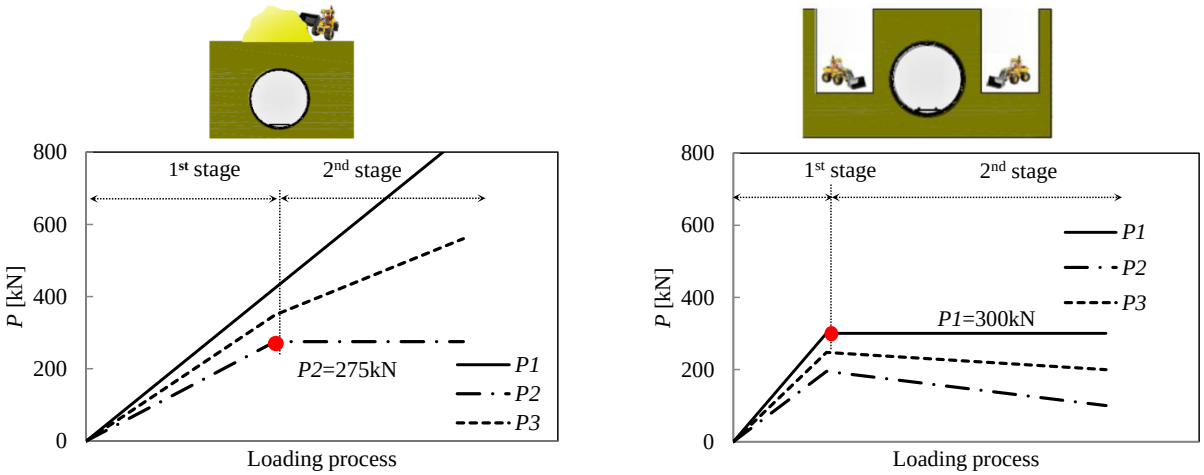

(a) Load case 1 (b) Load case 2

Fig. 4 Loading process of P1, P2, and P3

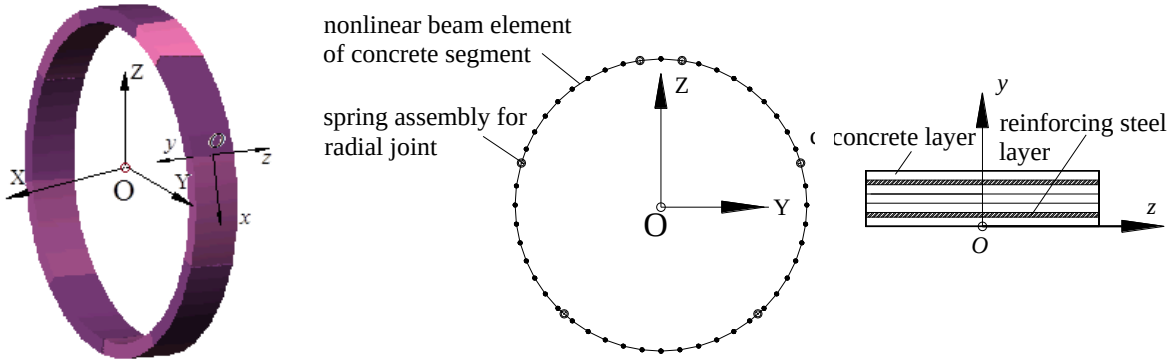

(a) Overview of a tunnel lining segment (b) FE-Model of the segment (c) Section of a layered reinforced concrete element

Fig. 5 Assembled macro-model representing a typical segmental lining

until the peak load was reached. After that, the test was continued under displacement control. Two different load cases were considered in the test.

Load case 1 represents overloading on the ground surface above the tunnel, as shown in Fig. 4(a). The loading process under load control consists of two stages:

(1) Gradually increase $P2$ to 275 kN (corresponding to the state that the soil reaches the passive earth pressure) with increasing $P1=P2/0.65$ and $P3=0.5(P1+P2)$ accordingly.

(2) Keep $P2$ constant at 275kN while increase $P1$ and $P3=0.5(P1+P2)$ until the lining structure reaches its ultimate capacity.

Load case 2 represents unloading on the both sides of the tunnel due to excavation, as shown in Fig. 4(b), the loading process under load control consists of two stages:

(1) Gradually increase $P1$ to 300 kN with increasing $P2=0.65P1$ and $P3=0.5(P1+P2)$ accordingly.

(2) Keep $P1$ constant at 300kN while reduce $P2$ and $P3=0.5(P1+P2)$ until the lining structure reaches its ultimate capacity.

3. Modelling of a segmental tunnel lining

3.1 Modelling concept of segmental tunnel lining

The model proposed for a segmental tunnel lining is a component-based macroscopic model, where the nonlinear behaviours of reinforced concrete lining segments and the radial joints between the segments can be captured. Comparing to a continuum mechanics-based microscopic model, such a model is highly computational efficient and has reasonable accuracy if calibrated carefully.

Two coordinate systems are adopted as shown in Fig. 5(a): a global coordinate system denoted as *XYZ* for the whole single-ring lining structure and a local coordinate system denoted as *xyz* for the cross-section of beam elements. In the local coordinate system, the *y*-axis points to the ring center and the *z*-axis is on the ring tangential direction. Fig. 5(b) describes the macro-model of the lining structure consists of fiber-discretized beam elements representing the reinforced concrete segments and spring-element-assemblies representing the radial joints connecting the segments. The beam element size is selected that the further refinement would not significantly change the simulation results. In this study, a total of 26 beam elements are used for the whole ring. Fig. 5(c) shows the cross-section of the lining segments is discretized into six layers:

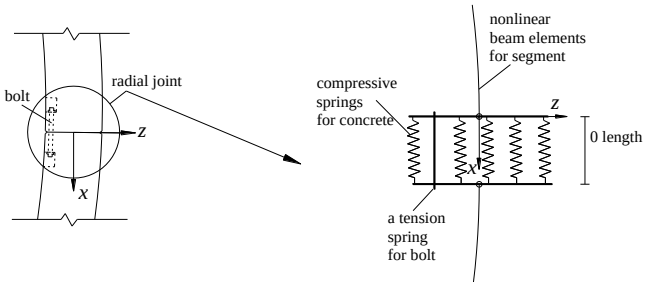

(a) Sketch (b) Detail

Fig. 6 Spring-assembly representation of a radial joint

four layers representing concrete and two layers representing the reinforcing steel. The material constitutive laws will be described in the next section. Inelastic responses of the lining structure as well as the axial load-moment interaction can be captured by the developed macro-model.

Fig. 6(a) shows a sketch of a radial joint of the specimen. The corresponding radial joint model is shown in Fig. 6(b). The model consists of multiple parallel zero-length nonlinear spring elements between two rigid elements, whose lengths are equal to the thickness of the reinforced concrete segments. The center nodes of the rigid elements are tied to beam-end nodes. The spring elements with compressive stiffness only are used to represent contact between two adjacent segments, while a single spring element is used to represent the connecting bolts. The axial force and bending moment are transferred through these idealized springs. The force versus displacement relationships of the spring elements will be discussed in a later section.

The proposed numerical model was implemented in the commercial software LS-DYNA (2007). The lining segments were modelled with Hughes-Liu beam elements. Concrete and steel materials of the segments were modelled using the No. 174 material model (MAT_RC_BEAM) in LS-DYNA. Discrete beam elements were used to model the zero-length nonlinear spring elements with the No. 119 material model (MAT_GENERAL_NONLINEAR_6DOF_DISCRETE_BEAM). The geometric nonlinearity was also included in the analysis.

3.2 Constitutive law used in the numerical simulation

The constitutive laws for concrete and steel materials of the reinforced concrete segments are similar to those adopted in an earlier study (Zhao *et al*. 2010). The concrete stress-strain relationship is shown in Fig. 7(a), which is similar to the concrete model proposed by Park and Paulay (1975). In compression, the stress and strain responses follow a parabolic curve up to the compressive strength σ_c, and then the stress decays linearly with increasing strain until the ultimate strength σ_{cu} is reached. Unloading is characterized by the initial stiffness followed by a degraded slope. In tension, a linear stress-strain behaviour is assumed until the tensile strength σ_t is reached. Thereafter the stress decays linearly with increasing strain. ε_c and ε_{cu} are the strains corresponding to σ_c and σ_{cu}, respectively. The steel

Table 1 Material properties of concrete and steel fibers used in simplified simulation

Concrete	σ_c (MPa)	σ_{cu} (MPa)	σ_t (MPa)	ε_c	ε_{cu}
	50	5	2.4	0.0023	0.0045
Steel	σ_y (MPa)	σ_{ult} (MPa)		ε_{sh}	ε_{ult}
	340	420		0.03	0.2

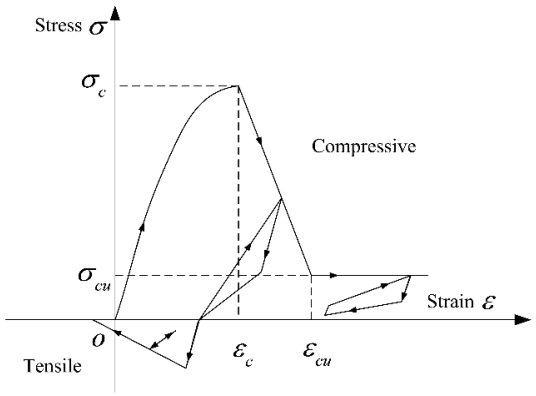

(a) concrete fibers

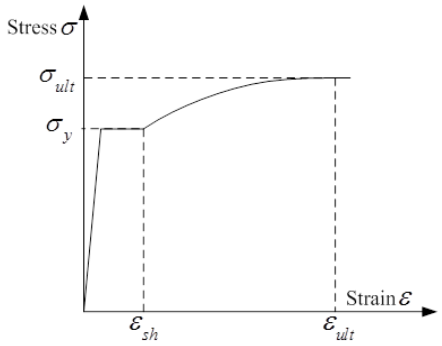

(b) steel fibers

Fig. 7 Stress-strain curves for segment cross section fibers

stress-strain relationship is described in Fig. 7(b), where the stress increases linearly before the yielding plateau at the yield strength σ_y, followed by a parabolic stress-strain curve between strains ε_{sh} and ε_{ult} until reaches the ultimate stress σ_{ult}. All material parameters mentioned above are listed in Table 1.

3.3 Modelling of radial joint

The force versus displacement relationship of the bolt spring is assumed to be trilinear as shown in Fig. 8, which is simplified from the tensile test result of the bolt. After the displacement reaches the ultimate value of 2.4 mm, the force-displacement curve becomes flat assuming the perfect plasticity. As shown in Fig. 9, there are 2-mm gaps between the two adjacent segments at the interior and exterior joint surfaces. Two end springs were used to capture bearing at the gap zones. Constrained interpolation is set for the corresponding nodes of the two end springs. In this way, geometry relationship of the ends of two adjacent segments is controlled to avoid overlap of the segments. Additional three springs were used to simulate contact at the core concrete zone.

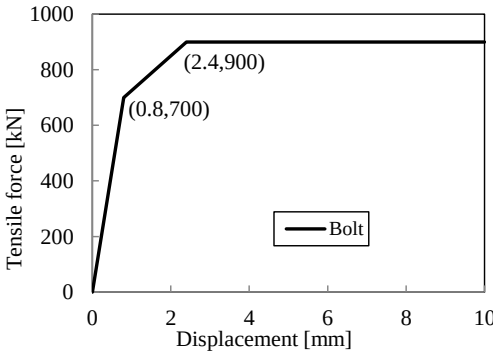

Fig. 8 Constitutive relationship for bolt spring

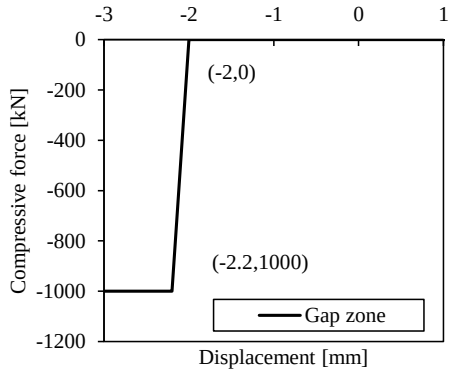

(a) Gap zone

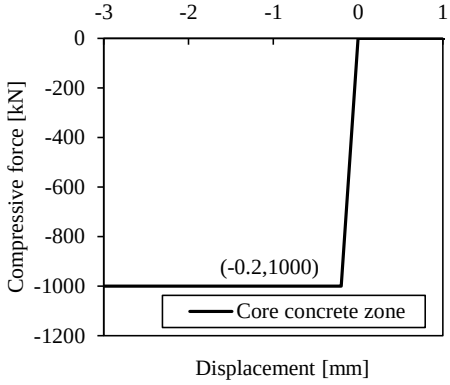

(b) Core concrete zone

Fig. 10 Force versus deformation relationships for concrete spring elements at radial joints

The force versus displacement relationships of the concrete spring elements at the gap and core concrete zones are described in Fig. 10(a) and Fig. 10(b) respectively. The force versus displacement relationship of the gap zone springs is similar to that of the core concrete zone springs with a 2-mm shift. A bilinear ideal elastoplastic curve is assumed to describe the force versus displacement relationships. The maximum compressive force of the spring element is calculated as the product of the concrete compressive strength σ_c and the corresponding tributary area. The displacement corresponding to the maximum compressive force is calculated based on the product of ε_c and the effective compressive depth, which is defined as the depth of the compressive zone when two adjacent segments contact.

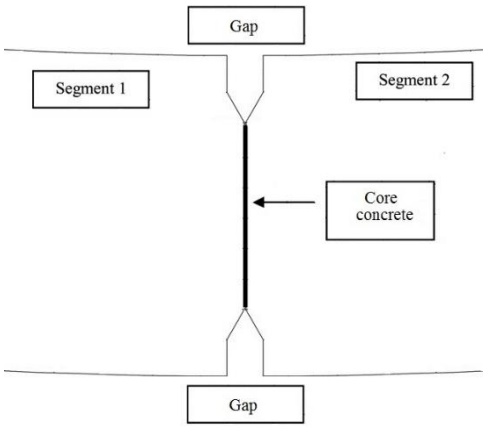

Fig. 9 Configuration of radial joints

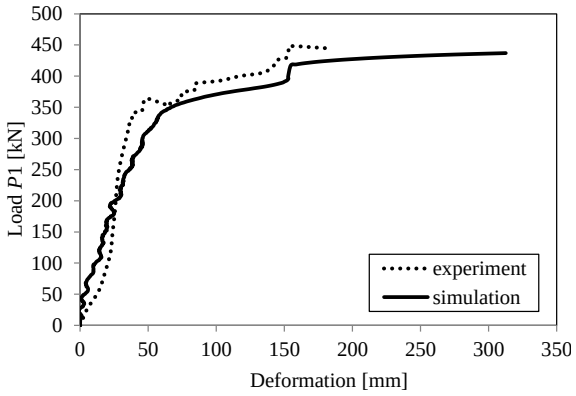

(a) Load P1 versus deformation

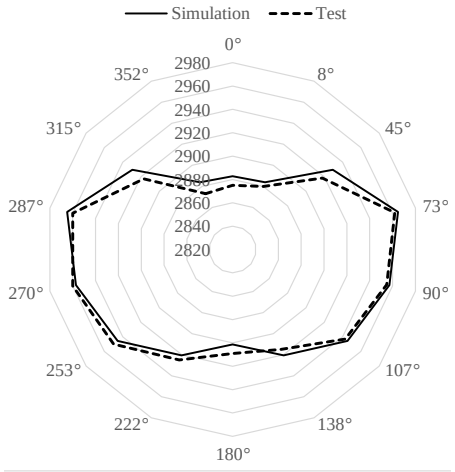

(b) Deformed linings when bolt yields

Fig. 11 Deformations obtained from experiment and from simulation

According to experimental data, the concrete compressive strains on the segment surface decreased with distance away from the radial joint. It also indicated that only insignificant strain was observed in the location where its distance to the radial joint exceeds the segment thickness at the elastic stage. Therefore, the effective compressive depth adopted herein equals to the segment thickness.

These spring elements represent axial and bending stiffness for joints. Shear stiffness representing the friction at the concrete interface and the shear of the bolt shaft is

ignored. The proposed simplified model of radial joint can capture the critical properties of mechanical behaviours of the joint. Shear test on joints can be avoided, bringing convenience and feasibility for engineers to simulate the lining structure.

3.4 Comparisons with test data

3.4.1 Load case 1: vertical overloading

Overall load-deformation response

Fig. 11(a) shows the measured and computed load $P1$ versus relative radial displacement between the top (point A in Fig. 2) and the bottom (point B in Fig. 2) of the lining structure. A linear load-displacement response was observed initially. The relative radial displacement started to increase rapidly after $P1$ exceeded 350 kN. It is noted that the post-yield stiffness was suddenly increased at a relative radial displacement of 166 mm. It indicates that as the large deformation of the lining structure 2-mm gaps shrink and full areas between the two adjacent segments at the joint contact and compress. The computed peak load of $P1$ is 437 kN, slightly less than the measured peak load of 448 kN. The overall deformed shapes of the lining structure at the first bolt yielded are also compared in Fig. 11(b). Good agreement is observed between the measured and computed results, indicating the proposed model can capture the overall load-deformation response with a reasonable accuracy

Opening at the joint

Opening at the joint is measured in the test by means of the displacement gauge at the interior or exterior joint surface between the two adjacent segments. The computed opening is calculated by deformations of the end springs at the gap zones. The computed and measured load P1 versus joint opening curves are plotted in Figs. 12(a), (b) and (c) for the six radial joints, noting that the joints at 8°, 73°, and 138° are symmetrical to the joints at 352°, 287°, and 222° respectively. In each plot, mean values were used for the joint opening. It is noted that the measured joint opening at 73°/287° is significantly larger than the joint opening at 8°/352° and 138°/222°. The computed results match well with the experimental data as shown in Figs. 12 (a) and (b), while the computed opening is less than the measured value at joint 138°/222°. Although with some discrepancy between the computed and measured results, the general trend of the development of joint opening is reasonably captured by the numerical model.

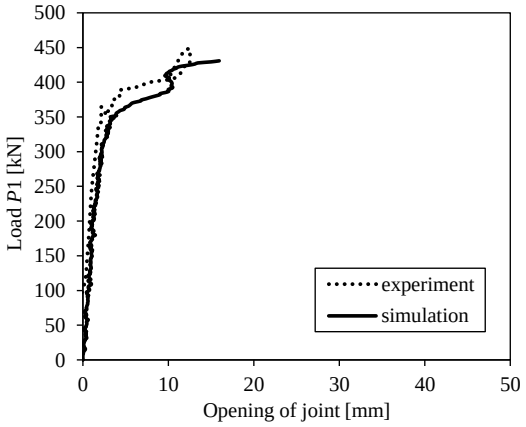

(a) For joints 8°/352°

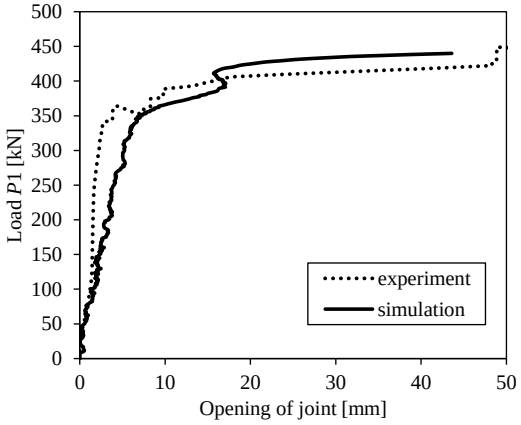

(b) For joints 73°/287°

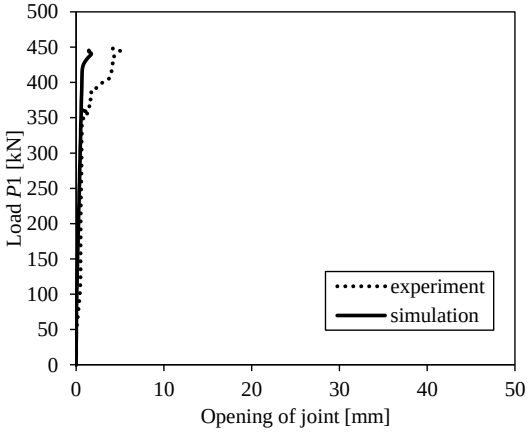

(c) For joints 138°/222°

Fig. 12 Load P1 versus opening of joint

Bolt strain of the joint

Figs. 13(a), (b), and (c) show the comparisons between the computed and measured bolt strains at the radical joints at 8°/352°, 73°/287°, and 138°/222° respectively. The mean values of joint opening were used in the plots due to symmetry. As consistent with the measured data, the computed results indicated that the bolts at the 8°/352° joints yielded with the maximum tensile strain about 0.005 and the bolts at the 138°/222° joints remained in elastic. Discrepancy at the initial slop of the P versus bolt strain curve shown in Fig. 13(a) may be due to the simplified assumptions used to define the force-displacement relationships for the joint springs.

The joint opening at 73°/287° is significantly larger than the joint opening at other locations. However, the bolt strain at 73°/287° is not the largest in Fig. 13. The bolt locates near the interior surface as shown in Fig. 6(b). The interior surface is in compression at 73°/287° joint. Therefore, the bolt strain at 73°/287° is smaller than that at 8°/352°.

3.4.2 Load case 2: lateral unloading

Overall load-deformation response

The load $P2$ versus relative radial displacement as well as the overall deformed shape of the lining structure at the

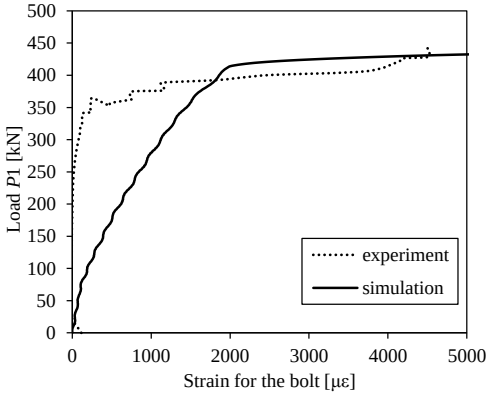

(a) For joints 8°/352°

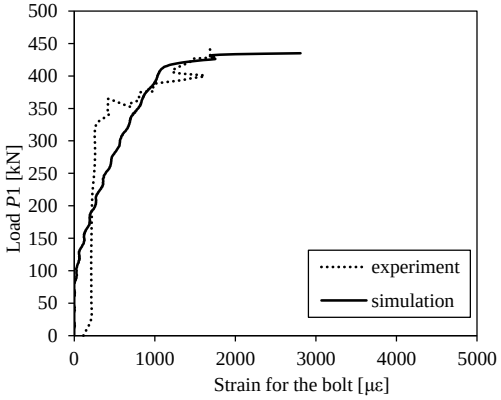

(b) For joints 73°/287°

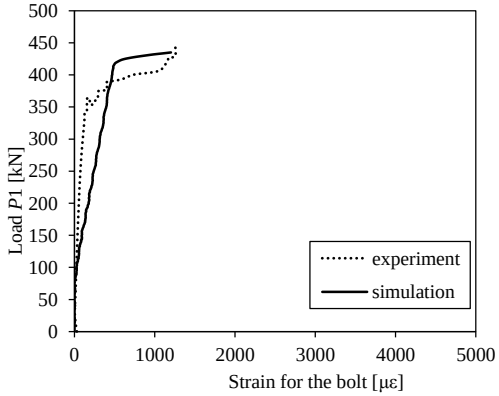

(c) For joints 138°/222°

Fig. 13 Load P1 versus strain for the bolts

first bolt yield is shown in Fig. 14. In general, good agreements between the computed and measured results are observed. A linear load-displacement response was observed when *P*2 increased to its peak load. With the reduction of *P*2, the relative radial displacement increased rapidly. It clearly indicates the collapse risk of the lining structure under the lateral unloading condition due to excavation activities.

Opening at the joint

Fig. 15 shows comparisons between the computed and measured load *P*2 versus joint opening curves. Same as observed in the load case 1, the joint opening at 73°/287° is significantly larger than the joint opening at other locations. As shown in Fig. 15, the predicted joint openings are

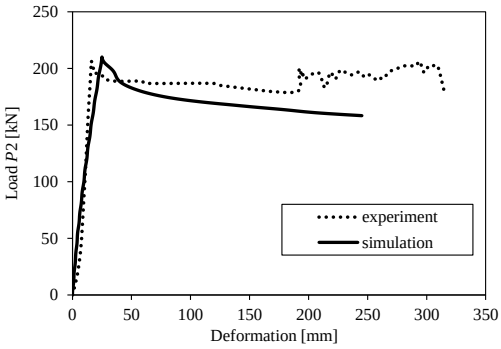

(a) Load *P*2 versus deformation

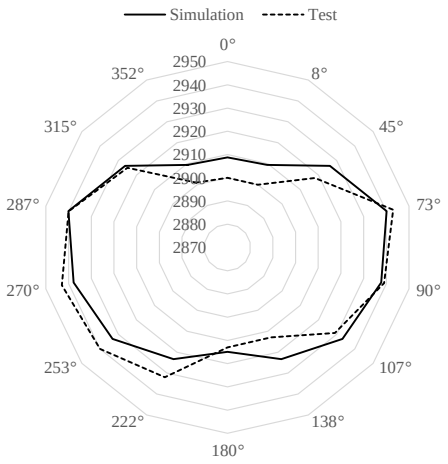

(b) Deformed linings when bolt yields

Fig. 14 Deformations obtained from an experiment and from simulation by the proposed model

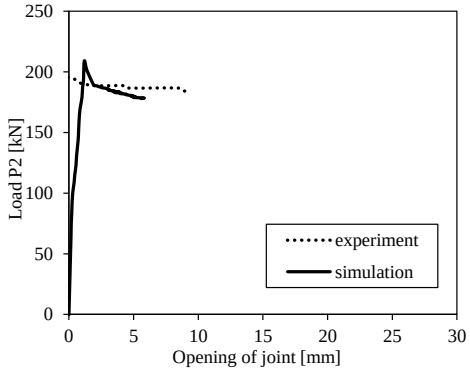

(a) For joints 8°/352°

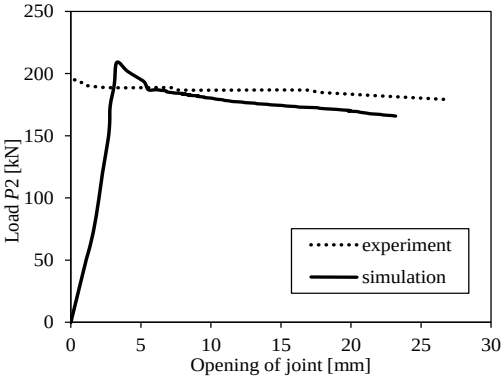

(b) For joints 73°/287°

Fig. 15 Load P2 versus crack width of joint

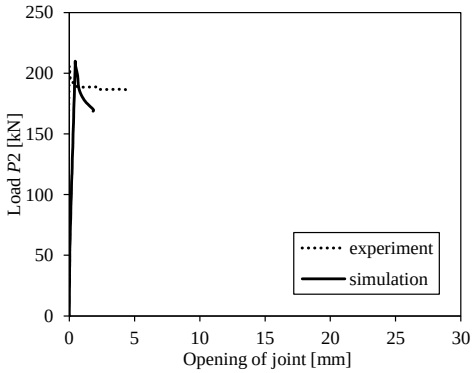

(c) For joints 138°/222°

Fig. 15 Continued

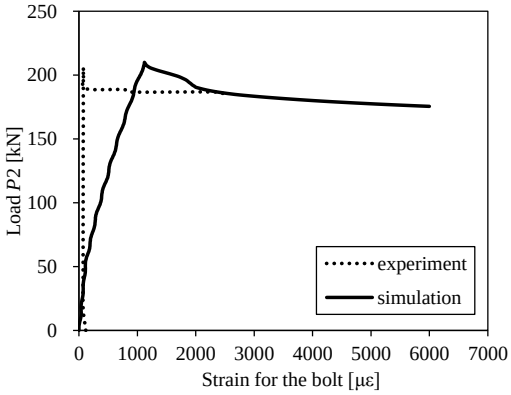

(a) For joints 8°/352°

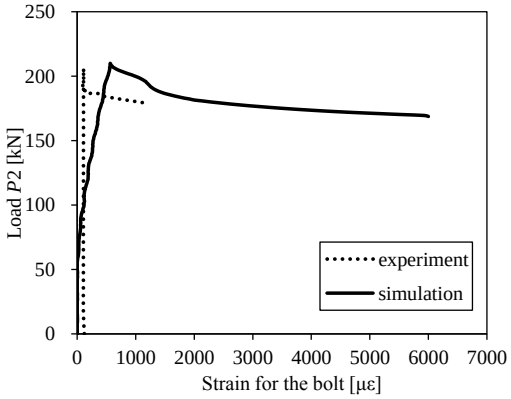

(b) For joints 73°/287°

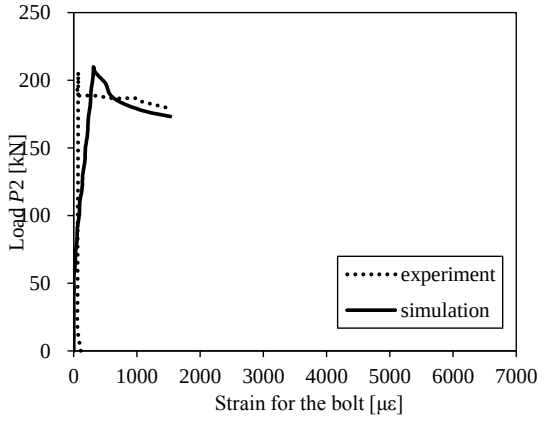

(c) For joints 138°/222°

Fig. 16 Load P2 versus strain for the bolts

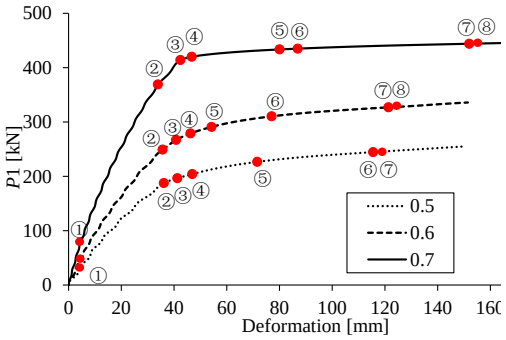

(a) Structural performance points

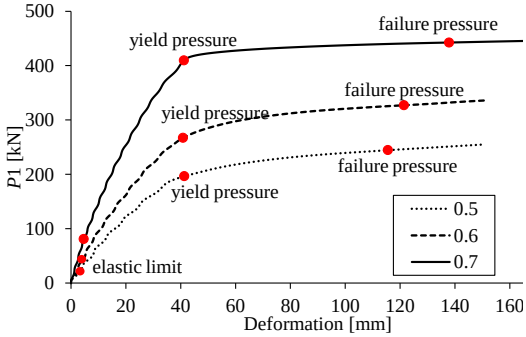

(b) Demarcation loads

Fig. 17 Structural performance points (a) and demarcation loads (b) of the lining for different values of the lateral pressure coefficient

slightly less than the measured data. However, the general trend of the development of joint opening is captured by the numerical model.

Bolt strain of the joint

Figs. 16(a), (b), and (c) show the comparisons between the computed and measured blot strains at the radical joints at 8°/352°, 73°/287°, and 138°/222° respectively. The computed and measured results agree well at the 138°/222° joints, while the numerical model predicted much larger blot strains than the recorded strains at the 8°/352° and 73°/287° joints. Although the simplified assumptions used to define the force-displacement relationships for the joint springs may contribute to such a discrepancy, it indicates that additional improvement is needed for the current model in the future study.

4. Parameter analysis

A parameter study was carried out to investigate factors that influence the performance of the lining structure. The same lining structure presented in the previous section were modelled and analysed under the overloading scenario with variations of four modelling parameters: the lateral pressure coefficient, the bolt strength, the bolt pre-tightening force, and the lining diameter.

4.1 Influence of the lateral pressure coefficient

The lateral pressure coefficient is the ratio of the lateral

load *P*2 to the vertical load *P*1. Depending on the property of surrounding soil, the lateral pressure coefficient of shield tunnels is in the range of 0.5 to 0.7. In this study, the lining structure is loaded to simulate the overloading scenario until collapse occurs. There different values of the lateral pressure coefficient are used in the analysis, namely 0.5, 0.6, and 0.7.

Fig. 17(a) shows the plots of the vertical load *P*1 versus the relative radical displacement between the top and bottom of the lining structure for three different lateral pressure coefficients. It is evident that the peak load of *P*1 as well as the initial stiffness increases significantly when increasing the value of the lateral pressure coefficient. The peak load is 444 kN with the lateral pressure coefficient of 0.7, an 82% increase comparing to the peak load of 244 kN with the lateral pressure coefficient of 0.5. The major performance points of the lining structure are summarized by the designated numbers representing the following observations during the load process: ① the bolts started to carry the tensile load; ② the bolts at the 8° joint reached the elastic limit; ③ concrete near the interior surface at the 73° joint crushed; ④ the bolts at the 73° joint reached the elastic limit; ⑤ concrete near the exterior surface at the 8° joint crushed; ⑥ the bolts at the 8° joint reached the plastic stage; ⑦ the bolts at the 73° joint reached the plastic stage; ⑧ the steel reinforcement inside the bottom segment (D) yielded, leading to failure of the lining structure. The performance points shown in Fig. 17(a) are in the same sequence for all curves. However, the corresponding deformations of the performance points ⑤, ⑥, ⑦, and ⑧ in the cases with the lateral pressure coefficients of 0.5 and 0.6 are smaller than those in the case with a lateral pressure coefficient of 0.7.

Fig. 17(b) shows the demarcation loads on the three curves including yield and failure load. The yield load is 412kN with the lateral pressure coefficient of 0.7, a 111% increase comparing to the peak load of 195kN with the lateral pressure coefficient of 0.5. While the displacement at yield point slightly varies for the three curves.

4.2 Influence of the bolt strength

Fig. 18 shows the plots of the vertical load *P*1 versus the relative radical displacement between the top and bottom of the lining structure for two different joint bolts, namely a M5.8 bolt and a M6.8 bolt. The elastic limit and the yield strength of the M5.8 bolt are 400 MPa and 500 MPa respectively. Those of the M6.8 bolt are 480 MPa and 600 MPa respectively. It can be seen that the shapes of the two curves are similar except that the transition from yielding to the plastic platform of the M6.8 bolt occurs slightly later than that of the M5.8 bolt.

The performance points shown in Fig. 18(a) are in the same sequence for the two curves. However, the corresponding deformations of the performance points ③ and ④ in the case with the bolt strength of M6.8 is smaller than that in the case with a bolt strength of M5.8. Fig. 18(b) shows the demarcation loads on the curves for two different bolt strengths. The yield load and the initial stiffness of the

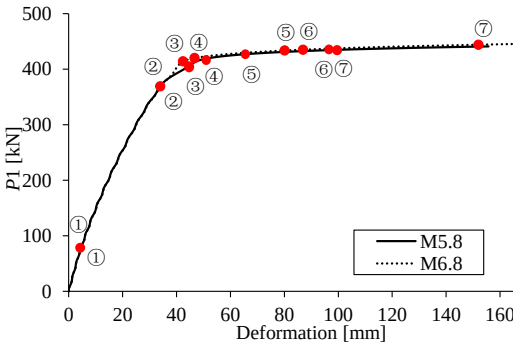

(a) Structural performance points

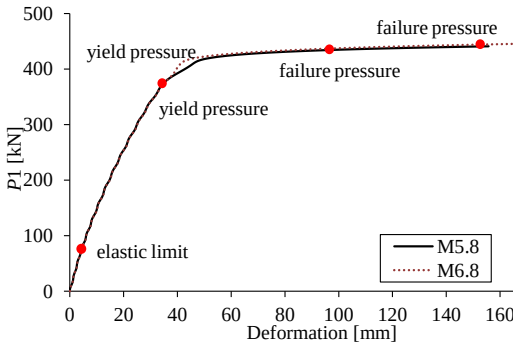

(b) Demarcation loads

Fig. 18 Structural performance points (a) and demarcation loads (b) of the lining for joint bolts with different strength

M5.8 and M6.8 joint bolt are the same.

4.3 Influence of the bolt pre-tightening force

Fig. 19 shows the plots of the vertical load *P*1 versus the relative radical displacement between the top and bottom of the lining structure for two different pre-tightening forces, namely 100 kN and 400 kN. The initial stiffness increases with the bolt pre-tightening force increased from 100 kN to 400 kN. The plastic platforms of the two curves differ very little.

The performance points shown in Fig. 19(a) are in the same sequence for the two curves. However, the corresponding deformations of the performance points ⑤, ⑥, ⑦, and ⑧ in the cases with the bolt pre-tightening force of 400 kN is smaller than that in the case with a bolt pre-tightening force of 100 kN. Fig. 19(b) shows the demarcation loads on the curves for two different bolt pre-tightening forces. The elastic limit of the lining with the bolt pre-tightening force of 600 kN has a 43% increase comparing to that of the ling with the bolt pre-tightening force of 400 kN. It is worth of mention that the deformations at yield and failure points decrease as the pre-tightening force increases.

4.4 Influence of the lining diameter

The influence of the lining diameter on the structural bearing capacity is also investigated. At present, the 6.2 m outer-diameter linings are most widely used in the Shanghai subway system. Recently, tunnel linings with a 6.6 m outer-

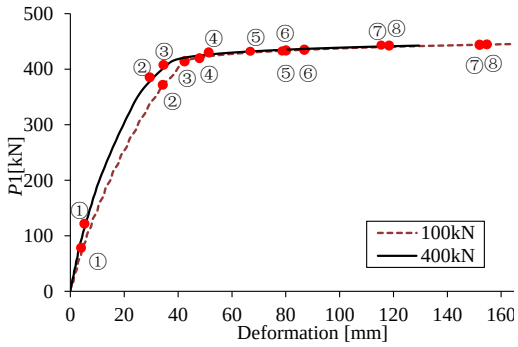

(a) Structural performance points

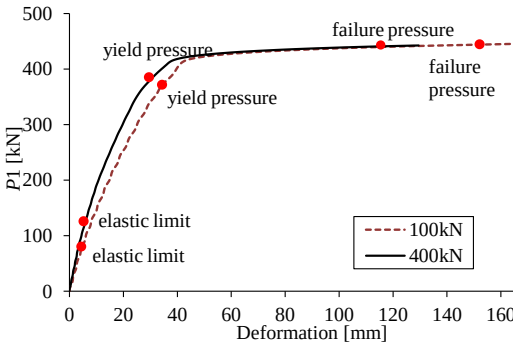

(b) Demarcation loads

Fig. 19 Structural performance points (a) and demarcation loads (b) of the lining for joint bolts with different the pre-tightening force

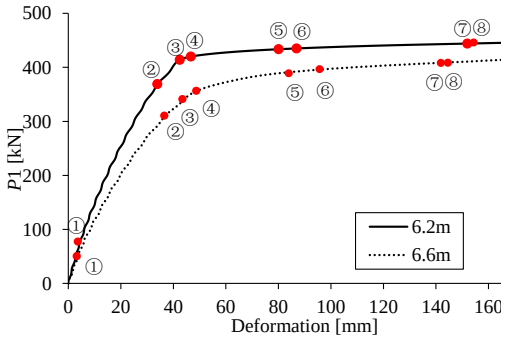

(a) Structural performance points

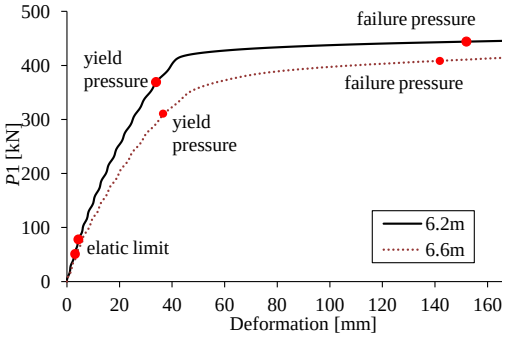

(b) Demarcation loads

Fig. 18 Structural performance points (a) and demarcation loads (b) of the lining for two different lining diameters

diameter are being considered more frequently. In the present study, outer diameters of 6.2 m and 6.6 m, respectively, are taken into account.

Fig. 20 shows diagrams of the vertical load $P1$ versus the displacement of the lining for two different lining diameters, 6.2 m and 6.6 m, respectively. It is seen that the initial stiffness and the peak load have increased significantly for the lining structure with smaller diameter. The order of the performance points on the two curves in Fig. 20(a) is the same for both cases. Fig. 20(b) shows the demarcation loads on the curves for two different lining diameters. The elastic limit of the lining with the lining diameter of 6.6 m has a 34% decrease comparing to that of the ling with the lining diameter of 6.2 m. The yield and failure load have a 15% and 6% decrease respectively.

5. Conclusions

A simplified approach for nonlinear analysis of reinforced concrete segmental tunnel linings was proposed. The method was validated by comparing the analysis results with the experimental results obtained from testing of a full scale lining. With help of the simplified simulation method, the influence of the lateral pressure coefficient, the bolt strength at the joints, the bolt pre-tightening force, and the diameter of the lining on the overall structural behaviour of the lining structure was investigated. Based on the findings from the present study, the following general conclusions are drawn:

1. The degradation of the structural performance of the lining in consequence of lateral unloading due to the excavation is more severe than that caused by vertical overloading. Therefore, more attention should be paid to the structural behaviour of the lining in case of unloading.
2. The lateral pressure coefficient has the greatest influence on the behaviour of the lining. The category and the properties of the soil and the distribution of the soil pressure should be taken into account in the simplified simulation of the lining structure.
3. Failure of the lining was found to follow a specific pattern, irrespective of different values of design: the bolts at the 8° joint reached the elastic limit and thus started yielding before the bolts at the 73° joint, and failure of concrete in compression of the 73° joint occurred prior to such failure of the 8° joint.

Acknowledgments

Financial support of this research by the National Natural Science Foundation of China (51578409 & 51208292), and the State Key Laboratory for Hazard Reduction in Civil Engineering Tongji University (SLDRCE14-B-27 & SLDRCE15-02) is gratefully acknowledged.

References

Ding, W.Q., Yue, Q.Z., Tham, L.G., Zhu, H.H., Lee, C.F. and

Hashimoto, T. (2004), "Analysis of shield tunnel", *Int. J. Numer. Anal. Meth. Geomech.*, **28**(1), 57-91.
Koyama, Y. (2003), "Present status and technology of shield tunneling method in Japan", *Tunnel. Underg. Space Technol.*, **18**(2), 145-159.
Koyama, Y., Konishi, S. and Sato, Y. (1997), "Study on special conditional shield tunnel segment design methods: very close twin tunnel", *J. Tunnel Eng. JPN Soc. Civil Eng.*, **7**, 273-278.
Liu, X., Bai, Y., Yuan, Y. and Mang, H.A (2015), "Experimental investigation of the ultimate bearing capacity of continuously jointed segmental tunnel linings", *Struct. Infrastr. Eng.*, 1-16
LS-DYNA (2007), *LS-DYNA Keyword User's Manual*, Livemore Software Technology Corporation, California, USA.
Naggar, H.E. and Hinchberger, S.D. (2008), "An analytical solution for jointed tunnel linings in elastic soil or rock", *Can. Geotech. J.*, **45**(11), 1572-1593.
Shiba, Y., Kawashima, K. and Obinata, N. (1989), "Evaluation procedure for seismic stress developed in shield tunnels based on seismic deformation method", *Proc. JPN Soc. Civil Eng.*, **404**, 385-394.
Tiberti, G., Plizzari, G.A., Walraven, J.C. and Blom, C.B.M. (2008), "Concrete tunnel segments with combined traditional and fiber reinforcement", *Proceedings of the fib 2008 Symposium*, Tailor Made Concrete Structures, Amsterdam, The Netherlands.
Vardakos, S. (2012), "Applied back-analysis methods for tunneling using numerical modelling", *46th U.S. Rock Mechanics/Geomechanics Symposium*, Chicago, Illinois, USA, June.
Yuan, Y., Jiang, X. and Liu, X. (2013), "Predictive maintenance of shield tunnels", *Tunnel. Underg. Space Technol.*, **38**, 69-86.
Zhao, H., Kunnath, S.K. and Yuan, Y. (2010), "Simplified nonlinear response simulation of composite steel-concrete beams and CFST columns", *Eng. Struct.*, **32**(9), 2825-2831

CC